Pergamon

0956-7151(95)00384-3

Acta mater. Vol. 44, No. 7, pp. 2963–2971, 1996

Published by Elsevier Science Ltd

1359-6454/96 $15.00 + 0.00

INTERFACE CRACKING PHENOMENA IN CONSTRAINED METAL LAYERS

M. Y. HE[1], A. G. EVANS[2] and J. W. HUTCHINSON[2]

[1]Materials Engineering Department, University of California, Santa Barbara, CA 93106 and
[2]Division of Applied Sciences, Harvard University, Cambridge, MA 02138, U.S.A.

(Received 14 August 1995)

Abstract—The deformation in thin ductile metal layers bonding elastic adherends is constrained. This constraint produces stress distribution with a large component of hydrostatic tension, such that the normal stress on the interfaces can greatly exceed the tensile flow strength of the layer material. The interaction of such stress fields with small incipient interface cracks is studied in this paper. Three models are analyzed: (a) pre-existing stationary cracks, (b) cracks which "nucleate" on a pre-loaded interface, and (c) cracks which grow along the pre-stressed interface, shielded by a thin plasticity-free region. A striking feature is a highly selective size dependence of the cracking process. A crack having a diameter roughly one half the layer thickness experiences significantly higher loading intensity than either larger or smaller cracks. This feature is related to recent experimental observations on interface debonding at thin ductile layers. *Copyright © 1996 Acta Metallurgica Inc.*

1. INTRODUCTION

A range of technologies involve thin metal layers bonded between elastic layers comprising ceramics, semiconductors or polymers. These applications include conductors in electronic devices, packages for multichip modules, diffusion bonded and brazed joints, multilayer protective coatings, etc. The stresses in the metal layers often exceed their yield strength when a small thermal or mechanical load is imposed. However, the resistance to plastic contraction of the metal supplied by the elastic layers leads to the build-up of large mean (hydrostatic) stresses in the interior. In turn, this produces normal stresses acting on the interface which can be many times the tensile flow strength of the metal. These large stresses cause the interface to be particularly susceptible to debonding and the metal prone to plastic cavitation. The focus in this paper is on the role of these stresses in the nucleation and growth of debonds on the interface. This occurs when the interfaces are relatively weak, with stresses less than about six times the tensile flow strength of the metal. When the interfaces are stronger, higher stresses arise and failure occurs by plastic cavitation.

Two examples illustrate the effect of constraint. (i) A round elastic rod, radius W, joined by a ductile layer of thickness t subject to axial load (Fig. 1). (ii) The distribution of mean stress ($\sigma_m = \sigma_{kk}/3$) ahead of a macroscopic crack in a thin metal layer joining two elastic solids (Fig. 2).

The material in the layer is taken to be elastic–perfectly plastic with tensile yield strength σ_Y and a Mises yield surface. The analogous plane strain solution has been provided in Ref. [1]. At the limit load, P_Y, with the layer fully yielded, the stress normal to the interface σ is approximately linearly distributed and varies from a maximum of about $(2/\sqrt{3})(W/t)\sigma_Y$ at the central axis to a minimum of about σ_Y at the outer edge. This maximum stress agrees closely with the computed value obtained using a finite element procedure (Fig. 1), described later.

The problem in Fig. 2 is small scale yielding in the sense that the plastic zone in the layer is assumed to be short compared with the length of the crack. Since the joint is loaded symmetrically, the behavior is governed by the mode I stress intensity factor K. Just ahead of the crack, the ratio σ_m/σ_Y is approximately three, typical of plane strain crack tip fields. However, the constraint causes the mean stress to increase further from the tip until it attains a peak. A sketch of the peak mean stress cross-plotted against its location ahead of the tip x^* is presented in the sub-plot in Fig. 2. These results, taken from Ref. [2], apply to a layer material with a strain hardening index of $N = 0.1$. The implication is that cavitation or debond nucleation may originate at some distance ahead of the crack tip (typically several layer thicknesses), whenever the mechanism of crack growth by tip extension is suppressed. Such behavior has been found experimentally for cavitation of strongly bonded Al/Al_2O_3 interfaces [3, 4] and for debond formation at weaker Au/Al_2O_3 interfaces [5, 6].

The above phenomena motivate the present study. In general, cavitation and interface debonding are

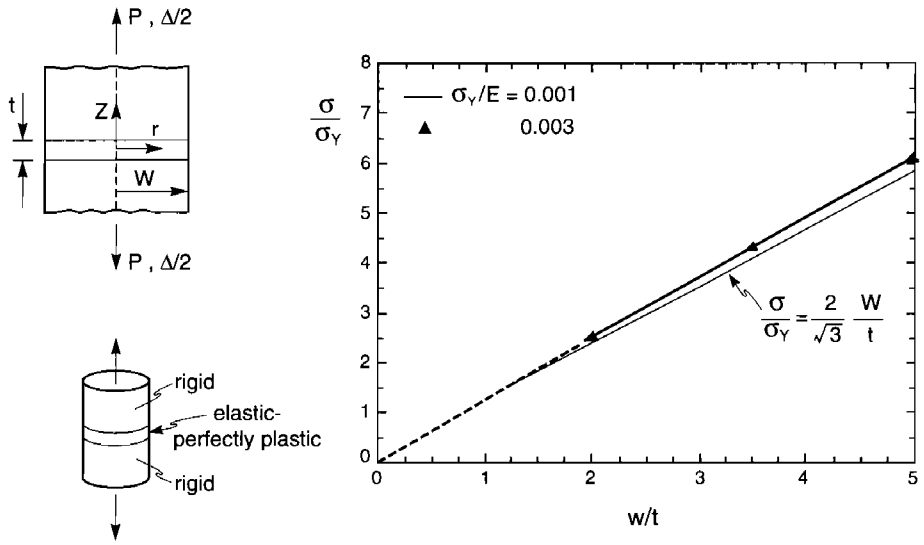

Fig. 1. Normal stress σ acting on the interface between the metal layer and rigid substrate at the axis of symmetry. The elastic–perfectly plastic layer is in the limit state: $\Delta E/t\sigma_y = 15$.

competing modes of fracture, because stress states which promote one also promote the other. The remote mean stress at which an isolated void in an unbounded solid expands without limit has been computed for an elastically incompressible solid with a piecewise linear/power hardening tensile stress–strain curve. The critical cavitation stress varies with σ_Y/E (with E as Young's modulus) and the strain hardening index N, as plotted on Fig. 3. Stress states other than purely hydrostatic tension have slightly different

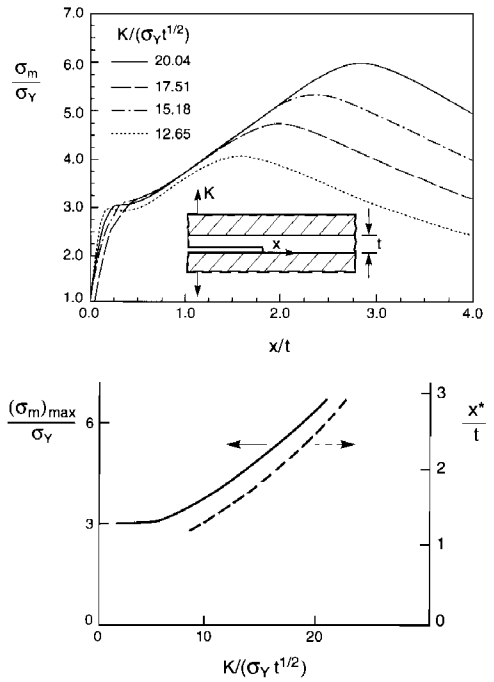

Fig. 2. Mean stress along the metal–substrate interface ahead of a long crack from Ref. [2].

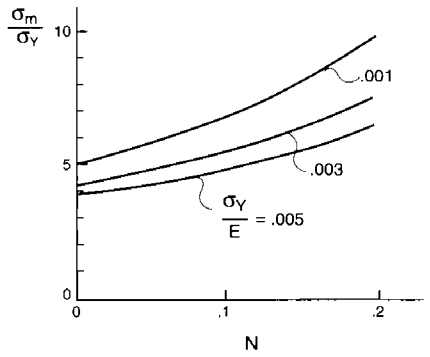

Fig. 3. Critical mean stress required for cavitation of an isolated void in an incompressible elastic–plastic solid with strain hardening exponent N.

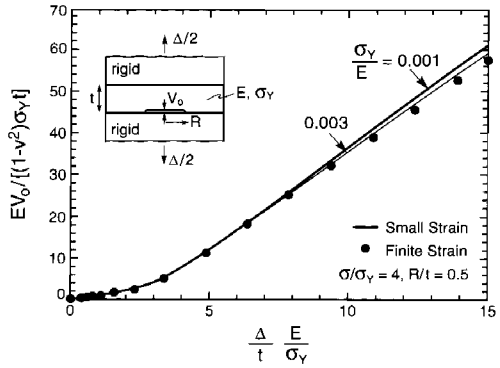

Fig. 4. Normalized opening at the center of a pre-existing penny-shaped crack with $R/t = 0.5$ at the layer–substrate interface as a function of imposed overall separation Δ. The radius W of the assembly is chosen such that the stress acting on the interface at the axis of symmetry is $\sigma/\sigma_Y = 4$.

critical cavitation stresses, but Fig. 3 can be used as a good approximation for general stress states [7]. The mean stress levels required for unstable cavitational growth of an interface void are somewhat higher [8]. Typically, the substrate constraint increases the cavitation stress by about σ_Y above that required for an interior void. Thus, the cavitation stress for an interface void is between 5 and $6\sigma_Y$ (depending on N and σ_Y/E). The stress acting on an interface attaching a thin ductile layer cannot exceed these levels, whenever voids are present. For this reason, the attention of this study is directed to interfaces subject to stress levels below about $6\sigma_Y$.

The models consider a small penny-shaped crack, radius R, located on the lower interface of the round bar in Fig. 1, with its center at the axis of symmetry (a blow-up of the crack region is included in Fig. 4). The material in the layer is elastic–perfectly plastic. Poisson's ratio ν is taken to be 0.3 in all calculations except those in Section 4. The adherends are taken to be rigid. The joint is loaded by imposing a separation Δ in the axial direction of the upper relative to the lower adherend. In the absence of the crack, the layer attains a limit stress at its center, approximately $(2/\sqrt{3})(W/t)\sigma_Y$, denoted σ, and given in Fig. 1. Three problems are addressed. In Section 2, pre-existing, stationary interface cracks are analyzed under increasing Δ. In Section 3, the effect of crack nucleation is modeled by pre-stressing the interface to σ, before a crack is present, and then "nucleating" a crack of radius R, with Δ held fixed. In Section 4, a crack located on the interface, pre-loaded to σ, is grown from zero size. In the latter, a thin plasticity-free region is imposed between the interface and the metal layer to model the effect of a dislocation-free zone, in the manner first introduced in Ref. [9]. In each of the models, the emphasis is on the response of the crack to the loading and on the effect of its size relative to the layer thickness.

A finite element analysis has been used to obtain the numerical results which follow. Some of the details are discussed in the Appendix. The elastic–perfectly plastic material in the layer is governed by incremental plasticity theory with a Mises (J_2) yield surface. Elastic unloading is rigorously taken into account in the calculations. This is not an issue for pre-existing cracks, but it has a major influence on the behavior of cracks nucleated on a preloaded interface as well as on cracks growing along a stressed interface.

2. PRE-EXISTING STATIONARY CRACKS

A penny-shaped crack of radius R is assumed to pre-exist on the interface between the ductile layer and the lower rigid block. The layer is loaded by monotonically displacing the upper and lower blocks by a relative distance Δ. The opening at the center of the crack, V_0, has been computed as a function of the average axial strain in the layer, Δ/t (Fig. 4). These

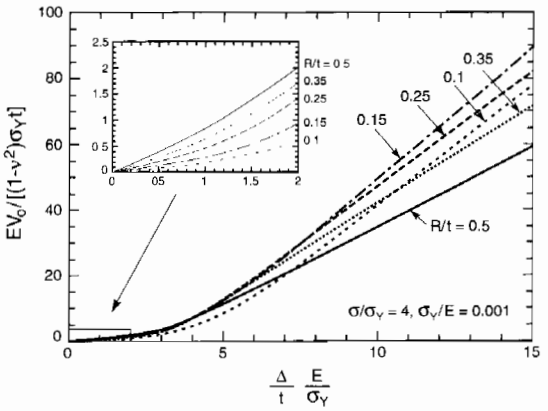

Fig. 5. Effect of the size of the pre-existing penny-shaped interface crack on the opening for $\sigma/\sigma_Y = 4$.

computations have been carried out with $R/t = 1$, $\sigma_Y/E = 0.001$ and 0.003, and $W/t = 3.25$, such that the limit stress in the center of the layer in the absence of the crack would be, $\sigma/\sigma_Y = 4$. The dots represent results computed using a finite strain formulation, while the solid curves represent small strain calculations. The difference in the predictions for the two formulations is small, even though the crack opening displacements become fairly large (almost $0.075t$ at the largest value of Δ). Consequently, the small strain formulation has been used to compute all other results. It can also be seen that the effect of σ_Y/E is very small when the normalizations in Fig. 4 are used.

The crack opening displacement at average layer strains, $(\Delta/t)(E/\sigma_Y) < 1$, is governed by elastic behavior. Whereas, for $(\Delta/t)(E/\sigma_Y) > 3$, the incremental changes in V_0 are dominated by the plastic response of the layer material. This is the range in which the stresses in the elastic–perfectly plastic layer have reached their limit state. The effect of the crack radius R on the opening at the center of the crack, (again, calculated with $\sigma/\sigma_Y = 4$ and $\sigma_Y/E = 0.001$), is summarized by Fig. 5. Within the elastic range (the insert in Fig. 5), the longer the crack, the larger the opening. This trend undergoes a dramatic reversal at layer strains within the plastic range. Now, the crack exhibiting the largest opening is that having normalized radius, $R/t = 0.15$. The opening at the center of the crack at three levels of σ/σ_Y (corresponding to the three values of W/t given by Fig. 1), computed at the same average layer strain, $(\Delta/t)(E/\sigma_Y) = 15$, well into the fully plastic regime, indicate a clear trend (Fig. 6). The higher the ratio of the reference stress to the yield strength, σ/σ_Y, the smaller is the crack that experiences the largest opening. For $\sigma/\sigma_Y = 5$, a crack of length $R/t \cong 0.1$ has the largest opening, almost twice that of a crack having radius five times larger. In this plot, we have chosen to normalize the opening displacement by the applied separation, Δ, thus emphasizing that the crack opening is highly magnified by the high triaxiality at the central axis of the joint.

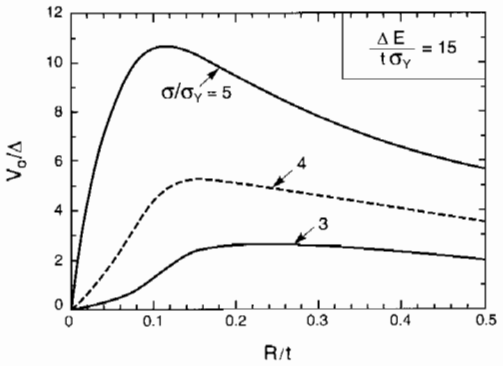

Fig. 6. Normalized opening of the pre-existing interface crack as a function of crack radius R for several levels of σ/σ_Y and for $\Delta E/(t\sigma_Y) = 15$.

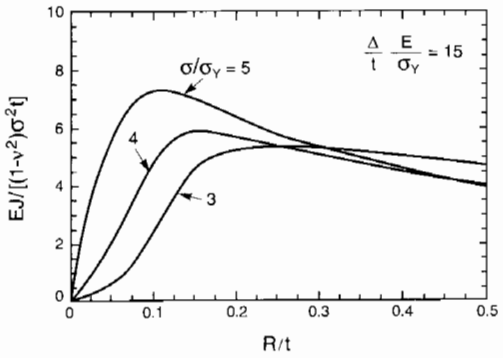

Fig. 7. Normalized crack tip intensity J of the pre-existing interface crack as a function of crack radius R for several levels of σ/σ_Y and for $\Delta E/(t\sigma_Y) = 15$.

To complete the picture, companion results are presented in Fig. 7 for the crack tip intensity, expressed by the J-integral, as a function of crack size, at separations which load the layer well into the plastic range. The path integral for J has been evaluated on a contour close to the tip, although there is little path dependence. The J displays the same trend with crack size as that for the opening displacement at the center of the crack. Note that the normalization of J uses σ^2 rather than σ_Y^2 and, therefore, the absolute value of J associated with the maxima in Fig. 7 increases sharply with increasing σ. When the stresses in the layer are in the elastic range, J can be identified with the energy release rate G, which is insensitive to W/t as long as $W \gg R$. A plot of the normalized G vs R/t is given in Fig. 8 for $W/t = 30$. The result for the penny-shaped crack approaches the limit for the long straight crack at a remarkably small value of R/t. The result for the long straight crack can be obtained by elementary energy methods and is given by $G = (1-2\nu)(1+\nu)\sigma^2 t/(2(1-\nu)E)$.

The unusual size-dependent crack phenomena in the plastic range are a consequence of the interaction of the cracks with the stress field in the layer. The high levels of mean stress characterizing the layers

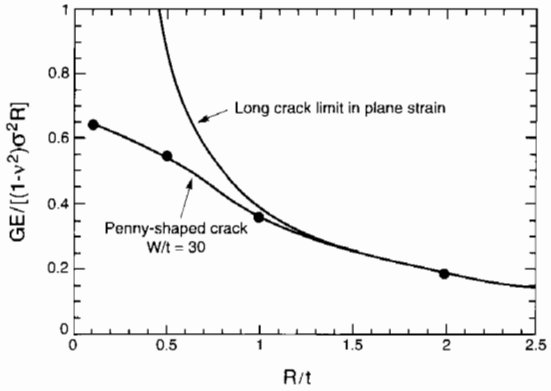

Fig. 8. Normalized energy release rate for the penny-shaped interface crack for an elastic layer for the limit $W \gg R$. The penny-shaped crack rapidly approaches the behavior of a straight plane strain crack.

(Figs 5 and 6) promote large crack openings. These openings create new volume which relieves the mean stress. Larger cracks provide enough new volume as they open to lower the mean stress throughout the central region of the layer. That is, the crack reduces the stress field which loads it. By contrast, a small crack creates insufficient volume to significantly affect the mean stress. Thus, the selection of smaller over larger cracks is not due to exceptional growth of the small cracks. Rather, it is a result of the self-unloading of larger cracks which thereby experience diminished growth.

3. CRACKS NUCLEATING AT FINITE SIZE ON A PRE-STRESSED INTERFACE

Suppose that a crack is nucleated at the center of the interface between the ductile layer and the lower adherend. The layer is first loaded well into the plastic range, $(\Delta/t)(\sigma_Y/E) = 15$. The stress on the interface at the center of the assembly is σ. Then the interface is allowed to "fail" over radius R in order to nucleate a crack. This is achieved by uniformly stepping down the traction on the interface over $r \leqslant R$ from σ to 0.

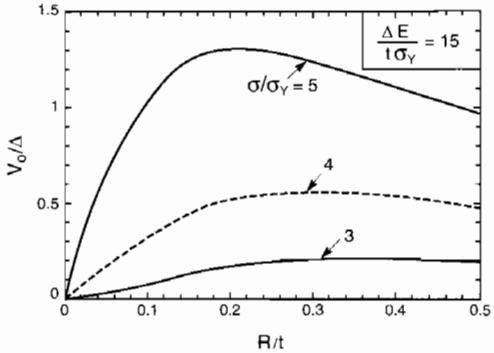

Fig. 9. Normalized opening of the "nucleated" penny-shaped interface crack as a function of crack radius R for several levels of σ/σ_Y and for $\Delta E/(t\sigma_Y) = 15$. (Contrast with Fig. 6.)

During this process, Δ is held fixed. The opening at the center of the crack V_0 increases monotonically. The normalized opening at the end of this nucleation process, V_0/Δ, is shown in Fig. 9, for the same three levels of pre-stress used in the last section. The crack opening displays a similar trend. At high σ/σ_Y, intermediate sized cracks have greater openings than large cracks.

The parameters for the three cases presented in Fig. 9 for the "nucleated" cracks are identical to those shown in Fig. 6. Note that there is a significant difference between the openings for the two types of crack. A pre-existing crack opens at its center almost ten times that of a "nucleated" crack having the same size, when loaded to the same Δ. This effect can be attributed to the strong history dependence of plastic deformation. The phenomenon is similar to that for voids [10], wherein a pre-existing void experiences many times the volume expansion of a void nucleated by failure of a particle interface, at the same stress. The material surrounding the pre-existing crack experiences continuous plastic loading, such that the volume expansion is virtually identical to that of a crack in a nonlinear elastic solid with the same tensile stress–strain curve (i.e. a deformation theory of plasticity). By contrast, the material surrounding the crack nucleated at the preloaded interface undergoes extensive elastic unloading and, consequently, the crack experiences much stiffer incremental behavior and less expansion.

4. CRACKS GROWING ON A PRE-STRESSED INTERFACE

The third model is introduced to elucidate the propagation behavior of a crack growing on a pre-stressed interface. The model employs a thin elastic strip of thickness h imposed between the interface and the elastic–plastic layer, as indicated in the insert in Fig. 10. The elastic modulus and Poisson's ratio of the strip are taken to be the same as those of the layer. This thin elastic strip was introduced in Ref. [9] as an

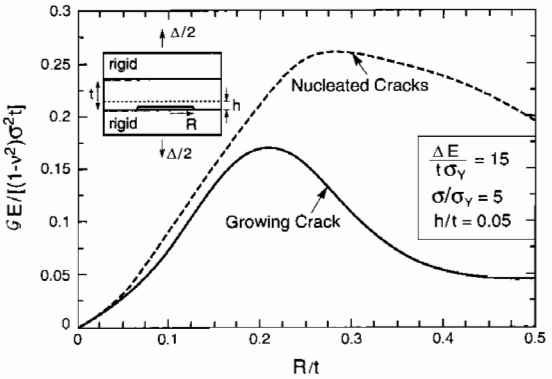

Fig. 10. Normalized energy release rate according to the SSV model for interface cracks which are either grown from zero size or nucleated at radius fixed R, under both cases with Δ applied before the introduction of the crack and subsequently held fixed.

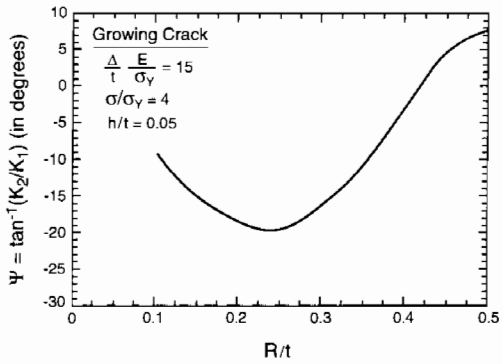

Fig. 11. Measure of mode mixity for the growing interface crack in Fig. 10.

effective way to model a dislocation-free region around the tip. The model gives rise to stress levels near the tip sufficient to produce atomic separation or cleavage. Such models, designated SSV, have the attractive feature that the crack tip is surrounded by elastic material and is fully characterized by the two stress intensity factors, K_I and K_{II}; or equivalently, an energy release rate G and mode mixity, Ψ. Plastic deformation occurs in the remaining bulk of the layer. In the calculations, the uncracked system is first loaded to a separation Δ with an associated interface stress σ at the center. (In using Fig. 1 to relate σ to W, one should now identify t as $t-h$, although the difference is small.) With Δ held fixed, a small crack is introduced on the interface and is then advanced incrementally by interface node release until it has grown to $R/t = 0.5$. At each crack radius, G and Ψ are computed. For comparison purposes, the SSV model has been used to nucleate cracks having finite radius on the pre-stressed interface, in the manner described in Section 3. The calculations in this section were carried out for a layer which is nearly incompressible ($\nu = 0.49$). While this makes little difference to the normalized values of G, it simplifies the interpretation of mode mixity because the second Dundurs parameter, β, is zero and thus Ψ does not depend on a reference length.

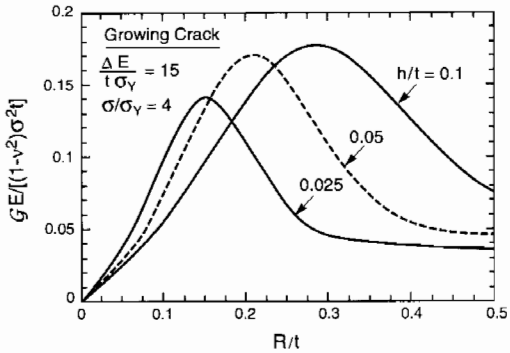

Fig. 12. Effect of the elastic strip height h in the SSV model on the normalized energy release rate of the growing interface crack.

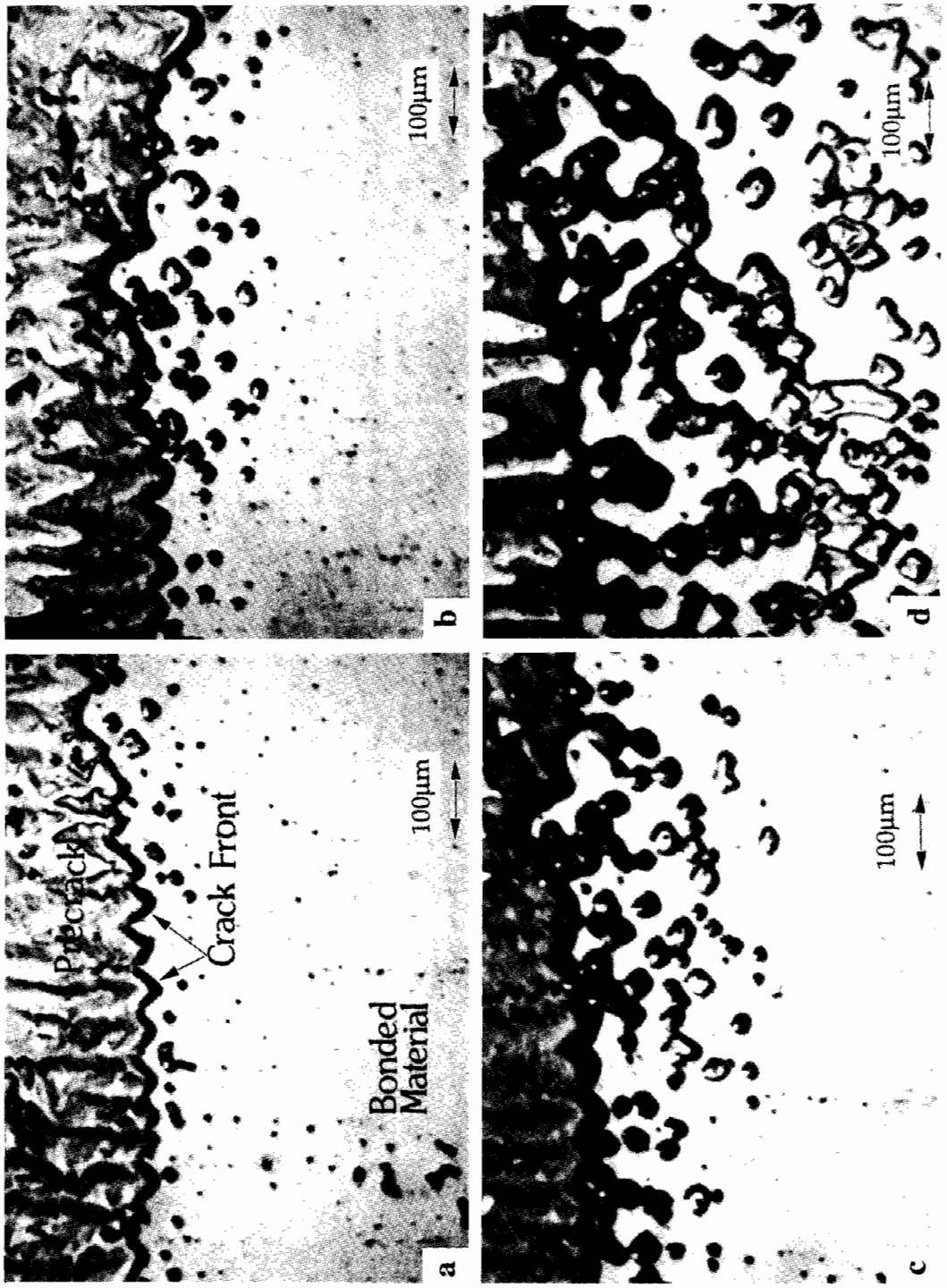

Fig. 13. A sequence showing debond patches that develop ahead of a precrack on an Al_2O_3/Au interface as the load increases, in the absence of stress corrosion.

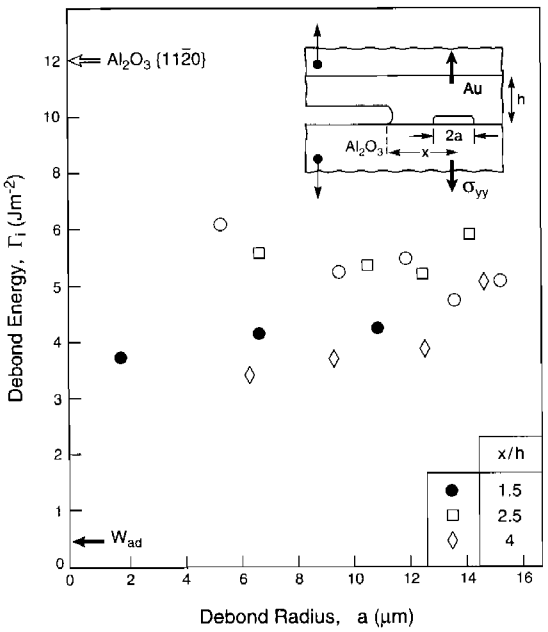

Fig. 14. The debond energies for the small debonds depicted in Fig. 13, calculated using the SSV results from Fig. 10 for $h/t = 0.05$.

The results are shown in Fig. 10 for a layer which has been pre-loaded to $(\Delta/t)(E/\sigma_Y) = 15$ and $\sigma/\sigma_Y = 4$. The thickness of the elastic strip has been taken to be one twentieth of the thickness of the layer. The computations have been carried out with $\sigma_Y/E = 0.001$, but the nondimensional parameters used in the plots capture essentially all of the dependence on σ_Y/E. The energy release rate of the crack which grows along the interface peaks at $R/t \cong 0.2$ and then falls sharply. The crack nucleated at fixed radius R shows a similar trend, but with a less abrupt drop-off after the peak. The mode mixity calculations for the growing crack (Fig. 11), reveal that the crack propagates under conditions which are essentially mode I.

The growing crack results (Fig. 10) indicate that an initial flaw of size $R/t \cong 0.1$ would propagate dynamically when G attains the interface toughness Γ_i. It would jump ahead until G drops below Γ_i. For the example in Fig. 10, this would occur when R/t reaches 0.3–0.4. Thereafter, the crack would advance stably under increasing Δ. In other words, once flaws begin propagating on the interface, they develop into debonds having radius about 0.3–0.4 times the thickness of the layer, but not smaller.

To apply the SSV model the thickness h of the plasticity-free elastic strip must be assigned. Hardening associated with intense strain gradients usually occurs over size scales ranging from 0.1 to 1 microns [11, 12]. It is expected that h would be of that order. Plots in Fig. 12 of the normalized G for the growing crack for three choices of h/t ranging from 0.025 to 0.1 indicate a relatively weak dependence on h/t over this range.

5. APPLICATION TO INTERFACE DEBONDING

Several oxide/metal interfaces exhibit failure by debonding of patches ahead of the precrack, particularly when stress corrosion is suppressed by excluding water vapor from the test environment. These systems include Al_2O_3/Au, Al_2O_3/Ni and Al_2O_3/Pt (Fig. 10). The most comprehensive measurements and observations have been made for Al_2O_3/Au. Qualitatively, the observations illustrate the phenomenon identified by Fig. 10. That is, debonds nucleate at flaws comprising small pores ~ 1 μm in diameter and "pop-in" to a radius $R/t \sim 0.5$. Subsequent growth occurs stably subject to increasing displacement. Video images of stable debond growth have been used [6] to estimate the energy release rate at debond growth by using the SSV results from Fig. 10. The reference stress relevant to the location of each debond is obtained from Fig. 2. The debond energies Γ_i, determined in this manner, are summarized on Fig. 14. These energies, being of order 8 Jm^{-2}, are much smaller than the macroscopic magnitudes that would be assessed by using the applied loads and the pre-crack length (60–100 Jm^{-2}) [6]. But, the Γ_i are larger than the work of adhesion ($W_{ad} = 1$ Jm^{-2}) and smaller than the cleavage energy for Al_2O_3 ($\Gamma_c = 12$ Jm^{-2}). The inferred Γ_i are thus in a physically acceptable range, given that interface debonding occurs in preference to oxide failure and that debonding is accompanied by plastic slip (dissipation) in the Au. Subsequent studies will use these Γ_i to understand the roles of plasticity and atomic decohesion in the debonding of metal/oxide interfaces.

6. CONCLUDING REMARKS

Some of the basic mechanics solutions for small axisymmetric debonds at the interface between a thin ductile layer and two elastic adherends have been derived. The most important phenomenon revealed by the analysis is an unloading effect that arises when the debond has diameter on the order of the one half layer thickness (and larger). This is attributed to the volume displaced by the plastic deformation that occurs around the debond. When an approach based on a plasticity-free zone (the SSV model) is used to simulate the associated debond propagation, it is found that this unloading causes the energy release rate G to exhibit a maximum, as the debond extends along the interface. Such G characteristics signify "pop-in" behavior, followed by a region of stable growth, wherein increasing displacements are needed to continue expansion of the debond. This finding rationalizes the behavior of small debonds observed to form on interfaces ahead of precracks at metal/oxide interfaces.

Preliminary application of the model to debonds measured on Au/Al_2O_3 interfaces has provided a rational measure of the fracture toughness Γ_i of this

interface in the absence of stress corrosion. The inferred Γ_i are about an order of magnitude larger than the work of adhesion, and about half the toughness of the Al_2O_3. An important role of plasticity in governing Γ_i is implied, consistent both with the model and with the experimental observations of slip traces on the Au fracture surfaces [6]. Further work is needed to relate this information to the fundamentals of the rupturing of the interface bonds.

Acknowledgements—This work is supported in part by the National Science Foundation under Grants MSS-92-02141 and DMR-94-00396, by the Office of Naval Research under Grant N00014-95-1-0183, and by the Division of Applied Science, Harvard University.

REFERENCES

1. R. Hill, *Mathematical Theory of Plasticity*. Oxford University Press (1950).
2. A. G. Varias, Z. Suo and C. F. Shih, *J. Mech. Phys. Solids* **39,** 963 (1991).
3. A. G. Evans and B. J. Dalgleish, *Acta metall. mater.* **40,** Suppl., S295 (1992).
4. W. E. King, G. H. Campbell, D. L. Haupt, J. H. Kinney, R. A. Riddle and W. L. Wien, *Scripta metall.*, in press.
5. I. Reimanis, B. Dalgleish and A. G. Evans, *Acta metall. mater.* **39,** 3133 (1991).
6. M. R. Turner and A. G. Evans, *Acta mater.*, **44,** 863 (1996).
7. Y. Huang, J. W. Hutchinson and V. Tvergaard, *J. Mech. Phys. Solids* **39,** 223 (1991).
8. V. Tvergaard, *Acta metall. mater.* **39,** 419 (1991).
9. Z. Suo, C. F. Shih and A. G. Varias, *Acta metall. mater.* **41,** 1551 (1993).
10. J. W. Hutchinson and V. Tvergaard, in *Fracture Mechanics: Perspectives and Directions (Twentieth Symosium), ASTM STP 1020* (edited by R. P. Wei and R. P. Gangloff) Philadelphia, 61, (1989).
11. N. A. Stelmashenko, M. G. Walls, L. M. Brown and Yu. V. Milman, *Acta metall. mater.* **41,** 2855 (1993).
12. N. A. Fleck, G. M. Muller, M. F. Ashby and J. W. Hutchinson, *Acta metall. mater.* **42,** 475 (1994).
13. C. F. Shih, B. Moran and J. Nakamura, *Int. J. Fracture* **30,** 79 (1986).
14. J. W. Hutchinson and Z. Suo, *Adv. appl. Mech.* **29,** 63 (1991).

APPENDIX

Finite element analysis

In the finite element analysis, a general purpose code, ABAQUS, was used, with close attention to mesh refinement. Four-noded axisymmetric elements are utilized with four integration points for each element. Refined meshes are placed around the interface and near the crack tip. A typical mesh for pre-existing crack with $R/t = 0.5$ is shown in Fig. A1, which contains 2048 four-node elements and 2189 nodes. A fine focused mesh was used at the crack tip to obtain accurate values for the J integral, which was calculated by the domain integral method [13] for ten contours. The maximum variation of J between contours is less than 1%.

For the growing crack shielded by a very thin plasticity-free region (SSV model), the crack tip is surrounded by elastic material. The crack opening displacements at a distance r behind the tip are given by [14]

$$\delta_y + i\delta_x = \frac{4\sqrt{2}}{(1+2i\epsilon)\cosh(\pi\epsilon)} \frac{(K_1 + iK_2)}{E_*} \sqrt{\frac{r}{\pi}}\, r^{i\epsilon} \quad \text{(A1)}$$

where

$$\frac{1}{E_*} = \frac{1}{2}\left(\frac{1}{\bar{E}_1} + \frac{1}{\bar{E}_2}\right) \quad \text{(A2)}$$

where $\bar{E} = E/(1-\nu^2)$ and material 1 is above the interface and material 2 is below. For the present case of rigid adherends, $\bar{E}_2 = \infty$, and

$$\frac{1}{E_*} = \frac{1}{2\bar{E}} \quad \text{(A3)}$$

In the calculations associated with the SSV model, Poisson's ratio ν was taken to be very close to 0.5 such that the second Dundurs' elastic mismatch parameter is nearly zero ($\beta = 0$), and also $\epsilon = 0$. The stress intensity factors K_1 and K_2 were

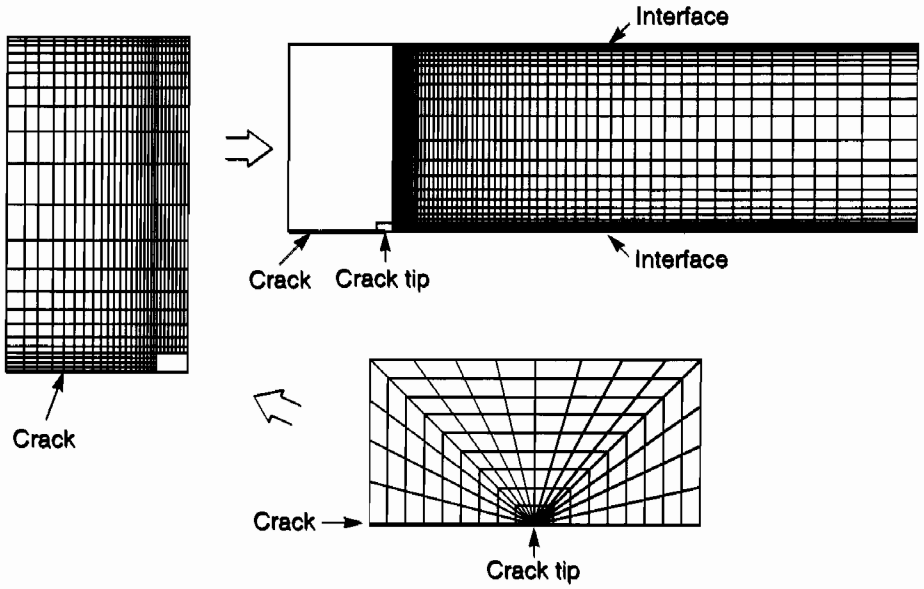

Fig. A1. Finite element meshes.

obtained from the crack opening displacements, δ_y and δ_x, by numerically adapting the formulae

$$K_1 = \lim_{r \to 0} \frac{E\delta_y}{2\sqrt{2}} \sqrt{\frac{\pi}{r}}$$

$$K_2 = \lim_{r \to 0} \frac{E\delta_x}{2\sqrt{2}} \sqrt{\frac{\pi}{r}} \tag{A4}$$

The mode mixity was then obtained using

$$\Psi = \tan^{-1}(K_2/K_1) \tag{A5}$$

The corresponding strain energy release rate is

$$G = \frac{(K_1^2 + K_2^2)}{2\bar{E}} \tag{A6}$$

The values for the strain energy release rate obtained by (A6) were compared with that calculated by the domain integral method and were found to be in very good agreement.

For the thin elastic strip a 98×8 rectangular mesh was employed with 40×8 uniform rectangular elements along the prospective crack path. The whole mesh for the growing crack problem contains 3920 elements and 4059 nodes. The J integral was calculated for seven contours in the elastic strip. The variation of J between contours was again less than 1%.